The 2010 M_W 6.8 Yushu (Qinghai, China) earthquake: Constraints provided by InSAR and body wave seismology

Zhenhong Li,[1] John R. Elliott,[2] Wanpeng Feng,[1,3] James A. Jackson,[4] Barry E. Parsons,[2] and Richard J. Walters[2]

Received 9 March 2011; revised 27 June 2011; accepted 7 July 2011; published 4 October 2011.

[1] By combining observations from satellite radar, body wave seismology and optical imagery, we have determined the fault segmentation and sequence of ruptures for the 2010 M_w 6.8 Yushu (China) earthquake. We have mapped the fault trace using displacements from SAR image matching, interferometric phase and coherence, and 2.5 m SPOT-5 satellite images. Modeling the event as an elastic dislocation with three segments fitted to the fault trace suggests that the southeast and northwest segments are near vertical, with the central segment dipping 70° to the southwest; slip occurs mainly in the upper 10 km, with a maximum slip of 1.5 m at a depth of 4 km on the southeastern segment. The maximum slip in the top 1 km (i.e., near surface) is up to 1.2 m, and inferred locations of significant surface rupture are consistent with displacements from SAR image matching and field observations. The radar interferograms show rupture over a distance of almost 80 km, much larger than initial seismological and field estimates of the length of the fault. Part of this difference can be attributed to slip on the northwestern segment of the fault being due to an M_w 6.1 aftershock two hours after the main event. The remaining difference can be explained by a non-uniform slip distribution with much of the moment release occurring at depths of less than 10 km. The rupture on the central and southeastern segments of the fault in the main shock propagated at a speed of 2.5 km/s southeastward toward the town of Yushu located at the end of this segment, accounting for the considerable building damage. Strain accumulation since the last earthquake on the fault segment beyond Yushu is equivalent to an M_w 6.5 earthquake.

Citation: Li, Z., J. R. Elliott, W. Feng, J. A. Jackson, B. E. Parsons, and R. J. Walters (2011), The 2010 M_W 6.8 Yushu (Qinghai, China) earthquake: Constraints provided by InSAR and body wave seismology, *J. Geophys. Res.*, *116*, B10302, doi:10.1029/2011JB008358.

1. Introduction

[2] On 13 April 2010 (UTC 23:49:37, Local time 7:49:37, 14 April 2010), a large earthquake (M_w = 6.8) struck Yushu county, Qinghai, China, causing 2,700 deaths and injuring over 12,000 people. This event occurred on the left-lateral Yushu fault that forms the western part of the Yushu-Garzê-Xianshuihe fault zone (Figure 1), one of the most active fault zones in eastern Tibet, which accommodates eastward movement of crustal material due to the ongoing collision of India with the Eurasia [*Gan et al.*, 2007]. Four large earthquakes are thought to have occurred on the Yushu-Garzê-Xianshuihe fault in the last 200–300 years (Figure 1), the last rupture in the locality of Yushu Town being 272 years ago [*Wen et al.*, 2003; *Zhou et al.*, 1997].

[3] On a regional scale, *Gan et al.* [2007] estimate an average slip rate of 14.4 mm/yr along the whole length of the Yushu-Xianshuihe fault using GPS data. A recent InSAR and GPS study suggests a slip rate of 9–12 mm/yr for the Xianshuihe fault at 101°E [*Wang et al.*, 2009].

[4] Focusing on the Yushu-Garzê strand of the fault (Figure 1), two previous studies indicate an along-strike variation in the Holocene left-lateral slip rate. *Wen et al.* [2003] used geological data at sites between 97° and 100°E (SE of Yushu city), and estimated an average slip rate of ~12 mm/yr for the past 50 ka. Based on remote sensing images and geological data, *Zhou et al.* [1996] reported that the average left-lateral slip rate on the Yushu-Garzê-Xianshuihe fault for 95°–99°E (NW of Yushu city) is at most 7 mm/yr. Assuming this strain accumulation rate, and that the previous seismic release on this portion of fault was 272 years ago, a slip deficit of almost 2 m existed before the Yushu earthquake.

[5] Preliminary teleseismic waveform analysis suggested that the earthquake was composed of two sub-events of up to 2.0 m slip on a 119° striking fault dipping SW [*Zhang et al.*,

[1]COMET+, School of Geographical and Earth Sciences, University of Glasgow, Glasgow, UK.
[2]COMET+, Department of Earth Sciences, University of Oxford, Parks Road, Oxford, UK.
[3]Institute of Geophysics, China Earthquake Administration, Beijing, China.
[4]COMET+, Department of Earth Sciences, University of Cambridge, Bullard Laboratories, Cambridge, UK.

0148-0227/11/2011JB008358

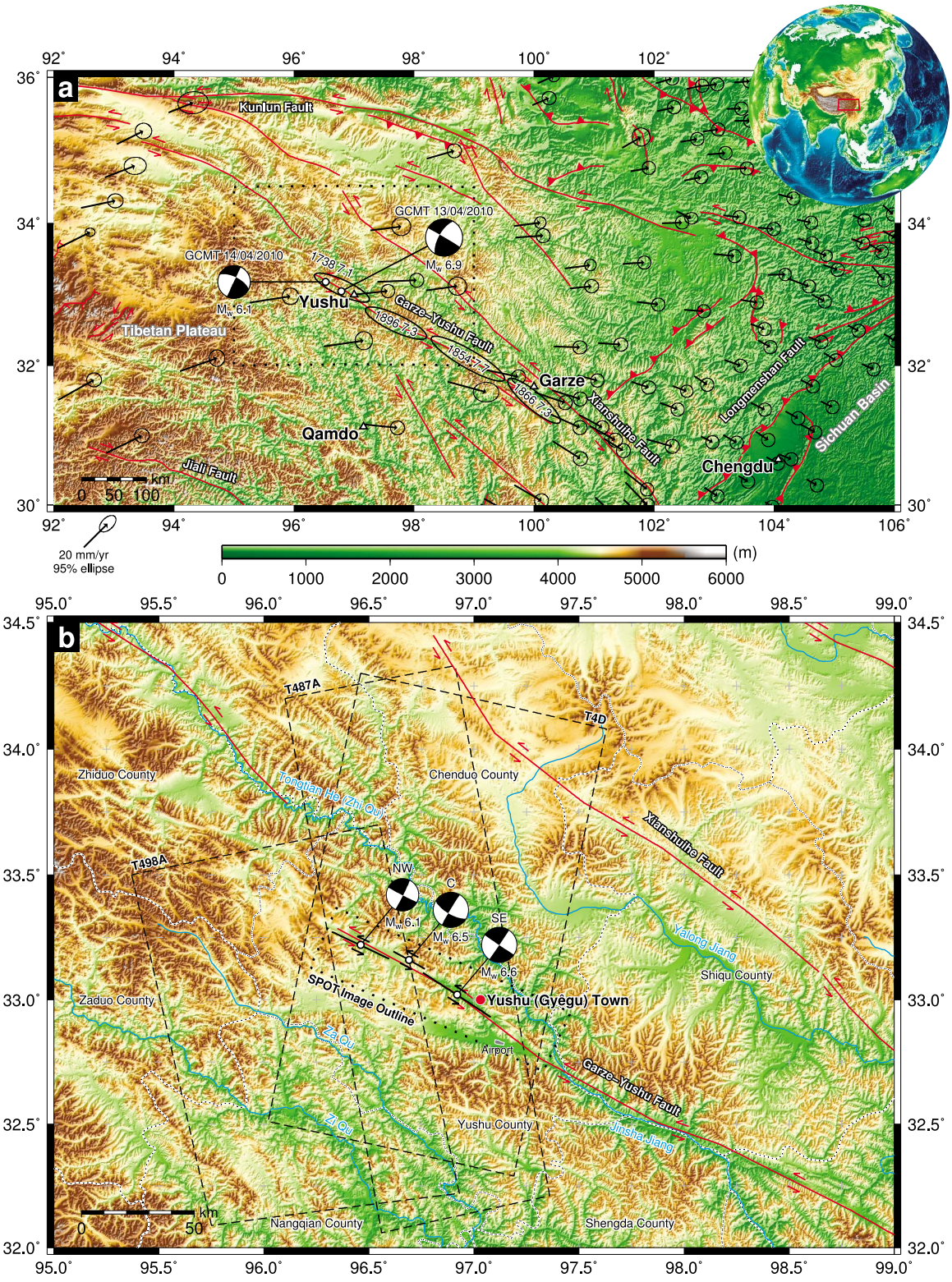
a
Kunlun Fault
GCMT 13/04/2010
M_w 6.9
GCMT 14/04/2010
M_w 6.1
1738 7.1
Yushu
Garze–Yushu Fault
1896 7.3
1854 7.4
Tibetan Plateau
Garze
1866 7.3
Xianshuihe Fault
Longmenshan Fault
Sichuan Basin
Qamdo
Chengdu
Jiali Fault
km
0 50 100
20 mm/yr
95% ellipse
(m)
0 1000 2000 3000 4000 5000 6000
b
T487A
T4D
Zhiduo County
Chenduo County
Tongtian He (Zhi Qu)
Xianshuihe Fault
T498A
NW
C
SE
M_w 6.1
M_w 6.5
M_w 6.6
Yalong Jiang
Shiqu County
Zaduo County
SPOT Image Outline
Yushu (Gyêgu) Town
Airport
Za Qu
Garze–Yushu Fault
Zi Qu
Yushu County
Jinsha Jiang
km
0 50
Nangqian County
Shengda County

Figure 1

Table 1. Seismological Fault Parameters From the Global CMT and USGS NEIC Catalog Solutions and Body Wave Modeling for the Main Shock on the 13th at 23:50, the Aftershock 95 Minutes Later on the 14th at 01:25, and a Small Foreshock 130 Min Before the Main Shock at 21:40[a]

Model	Strike (deg)	Dip (deg)	Rake (deg)	Longitude (deg)	Latitude (deg)	Depth (km)	Moment ($\times 10^{18}$ Nm)	M_w
				Main Shock 13 April 23:50				
Global CMT	120	90	−13	96.82	33.10	20	25	6.9
	210	77	−180					
USGS NEIC BW	298	88	4	96.53	33.16	16	13	6.7
	208	86	178					
Body Wave	117	77	351			6	20	6.8
	208	82	−166					
				Aftershock 14 April 01:25				
Global CMT	296	65	2	96.53	33.18	18	1.6	6.1
	205	89	155					
				Foreshock 13 April 21:40				
Global CMT	116	81	−19	96.71	33.08	27	0.03	4.9
	209	71	−171					

[a]Times and dates are UTC.

2010]. An M_w 4.9 foreshock occurred just over two hours before the main shock and an M_w 6.1 aftershock occurred less than two hours afterwards (Table 1).

[6] In order to improve our understanding of the nature of the faulting, we used a variety of sources of information to determine the fault trace for the Yushu earthquake, and modeled its slip distribution by combining radar interferometric measurements of surface displacements with body wave seismology.

2. InSAR, Optical Image and Seismological Constraints on Faulting

2.1. Interferometric Line-of-Sight Displacements

[7] On 20 April, we made available the first precise fault location and geodetic source model for the earthquake, determined with an ALOS coseismic interferogram (http://yushu.ges.gla.ac.uk and http://comet.nerc.ac.uk/current_research_yushu.html). This preliminary analysis was completed within 3 days of the first post-event ALOS PALSAR acquisition (including a 2-day delay for data delivery).

[8] In this study, three coseismic interferograms were formed from ALOS PALSAR and ENVISAT ASAR images (Table 2) using the JPL/Caltech ROI_PAC software (version 3.1 beta) [*Rosen et al.*, 2004]. The topographic phase contribution was removed using a version of the Shuttle Radar Topography Mission (SRTM) 3-arcsecond (~90-m) spacing digital elevation model (DEM) that has the voids filled with other data sources [*Jarvis et al.*, 2008], and the interferograms were unwrapped using the SNAPHU algorithm [*Chen and Zebker*, 2000] to obtain line-of-sight (LOS) displacements.

[9] Figure 2a shows a mosaicked pair of ascending interferograms, both rewrapped at 11.8 cm. ASAR Track 498 covers the northwest end of the ruptured fault of the Yushu earthquake, while PALSAR Path 487 covers both ends of this fault. The ASAR coseismic interferogram agrees well with the PALSAR one (Figure S1 in the auxiliary material).[1] The mosaic shows asymmetric, two-lobe, deformation in the SE segment while there is only one clear lobe of deformation in the NW segment (Figure 2a). In the SE segment, there is one fringe more of LOS deformation to the north than to the south; however, in the NW segment, there are 1–2 fringes more of LOS deformation to the south than to the north. The asymmetric feature indicates that the Yushu fault may comprise multiple segments and different segments may have different dip angles.

2.2. Azimuth and Range Displacements From SAR Image Matching

[10] Range and azimuth displacements can be estimated by matching two radar amplitude images using a cross-correlation method [*Michel et al.*, 1999; *Pathier et al.*, 2006]. SAR displacements determined in this way have two distinct advantages over conventional InSAR techniques: (1) they

[1]Auxiliary material data sets are available at ftp://ftp.agu.org/apend/journal/2011JB008358. Other auxiliary material files are in the HTML. doi:10.1029/2011JB008358.

Figure 1. (a) Topographic map of eastern Tibet, showing the location of the 2010 Yushu earthquake. The focal mechanisms for the main shock on 13 April and aftershock on 14 April are from the Global Centroid Moment Tensor (GCMT) catalog. Black vectors represent GPS velocities relative to a Eurasian reference frame with ellipses denoting 2σ errors [*Gan et al.*, 2007]. Red lines show previously mapped regional-scale faults [*Taylor and Yin*, 2009]. Approximate locations and extents of historical earthquakes are shown as ellipses with year and magnitude indicated [*Zhou et al.*, 1997; *Wen et al.*, 2003]. Dashed box indicates region covered in Figure 1b. Inset globe shows region of eastern Tibet delineated in Figure 1a (red rectangle). (b) Enlarged topographic map of the Yushu-Garzê-Xianshuihe fault systems. Focal mechanisms derived from InSAR modeling are shown in black for the northwestern (NW), central (C) and southeastern (SE) segments (solid lines). Dashed rectangles indicate the coverage of ALOS PALSAR (Track 487) and Envisat ASAR (Tracks 4 and 498). Dotted box indicates the SPOT image coverage in Figure 3. County borders are marked by black and white dotted lines.

Table 2. SAR Data Used in the InSAR Analysis[a]

Satellite	Track	Inclination	Master (YYMMDD)	Slave (YYMMDD)	ΔT (days)	ΔPT (days)	$B_\perp$ (m)	Inc (deg)	Data pts	$RMS^{(1)}$ (cm)	$RMS^{(2)}$ (cm)
ALOS	487	Ascending	100115	100417	92	4	712	38	2344	1.80	1.67
ENVISAT	498	Ascending	100215	100426	72	13	8	23	1610	0.46	0.44
ENVISAT	004	Descending	041005	100601	2065	48	91	23	1351	1.17	1.09

[a]Columns show satellite platform (ALOS = PALSAR, ENVISAT = ASAR), track number, satellite direction (ascending or descending), pre- and post-seismic acquisition dates, time interval ΔT, post-seismic interval ΔPT, perpendicular baseline $B_\perp$, incidence angle (Inc) in the center of the scene, number of data points in inversion, and the RMS difference between the interferogram and model for the uniform (1) and distributed slip with varying rake (2).

provide an unambiguous measurement of the surface displacement, and (2) the presence of macroscopic surface features such as ridges, lake shorelines or roads often means the technique works successfully even in regions that are incoherent in the corresponding interferogram. However, the data sets tend to be very noisy in the far-field. Therefore we use the location of offsets in these displacements only to provide a priori constraints on the fault geometry. We derive displacements from the full-resolution single-look complex (SLC) PALSAR images (3.5 m in azimuth, 4.7 m in slant range for images) at 16 pixel intervals in both azimuth and range, using overlapping matching windows of 64 by 64 pixels.

[11] The azimuth and range displacement maps (Figure 2) offer a comprehensive picture of the location of fault rupture of the Yushu event. The azimuth displacements are particularly useful for constraining the fault geometry, with a peak along-track offset of ~1.7 m across the fault observed for the southeastern segment (Figure 2b, red arrows).

2.3. Locating the Fault Trace With SAR and SPOT Imagery

[12] An accurate knowledge of the surface location of the fault not only provides invaluable guidance for fieldwork, but also provides a strong constraint on earthquake source models derived from geodetic data, both by reducing the number of unknown parameters and by preventing biases due to fault mislocation.

[13] The northwest end of the Yushu fault can be easily identified from the ASAR T498 coseismic interferogram (Figures 2a and S1a), and the southeast end from the PALSAR T487 interferogram (Figures 2a and S1c). Due to the generally good coherence at both C- and L-band, the fault location can be traced easily by combining offsets in the SAR matching displacements (Figure 2) and phase discontinuities in the interferograms (Figure S1c), confirmation often being provided by low interferometric coherence along the fault (Figures S1b and S1d).

[14] This fault can also be traced by analyzing geomorphic features in preseismic SPOT5 optical images (Figure 3) covering the length of the 80 km rupture. The fault is marked by sharp changes in incision, clear breaks in slope, and left-lateral offsets of many streams and valleys crossing the fault. The fault trace on the SPOT images agrees with the location of offsets in displacement to better than 500 m except in the vicinity of the town of Yushu, where the surface rupture veers up to 1.5 km away from the topographic trace of the fault.

[15] (1) SE segment: Figure 3f shows two left-lateral offsets in this region; a river that is offset by ~400 m and a small incised valley that is offset by ~50 m. On the SE segment, SAR interferometric phases (Figure 4) and SAR range and azimuth displacements (Figure 2) suggest slip across the fault of up to 1.5 m and 1.7 m respectively, and coherence is nearly lost close to the fault (Figure S1d). These observations clearly imply that the fault ruptured to the surface. Our SAR analysis suggests the total length of the surface rupture is at least 30 km, which agrees well with the field data collected by the Chinese Earthquake Administration (a total length of 31 km) [*Chen et al.*, 2010].

[16] (2) Central segment: Figure 3e shows stream offsets of up to ~200 m in the central segment of the fault, where the fault trace is marked by similar geomorphological features as those found on the SE segment. However, the phase is smoothly continuous (Figures 2a, 4b, and S1b) with relatively high coherence (0.25~0.50, Figure S1d), suggesting the slip remained buried on this segment. This conclusion is also supported by the continuous SAR azimuth and range displacements across this segment (Figures 2b and 2c).

[17] (3) NW segment: Figure 3d shows the northwestern end of the fault, where the geomorphological expression of the fault is the weakest, and no offsets can be seen. The fault trace here is marked only by a change in incision and a break in slope in the preseismic SPOT image. Continuous phase and relatively high coherence can be observed in Figures S1c and S1d, respectively. Profile A-A′ (Figure 4) shows a sharp left-lateral offset of 50 cm over a short length scale of about 200–300 m, suggesting that that the rupture nearly broke the surface. It is reported that no clear surface rupture was observed in the field in the NW segment except for a 2 km surface rupture at the SE end of the Longbao Lake [*Chen et al.*, 2010]. We originally neglected this small 2 km section when detecting the surface rupture using SAR observations. This is because the fault passes underneath Longbao Lake (Figures S1b and S1d), where low coherence and discontinuous phase were to be expected in the surrounding areas. On closer inspection of coherence maps over the 2 km surface rupture (denoted by a green arrowhead in Figure S1d), it is found that (1) the 2 km section is not covered by water. If it was in the lake, there would be no coherence in either L-band or C-band interferograms, but L-band data is coherent (Figure S1d) while C-band data is incoherent (Figure S1b); and (2) the phase is discontinuous, implying there is a small surface rupture along this section of the fault.

2.4. Body Wave Seismology

[18] To provide additional constraints on the earthquake source parameters (Table 1), teleseismic long-period waveforms were also modeled. The minimum misfit solutions for *P* and *SH* waves are given in Figure 5. We selected broadband seismograms from stations that are part of the Global Digital Seismograph Network (GDSN) and are optimally distributed

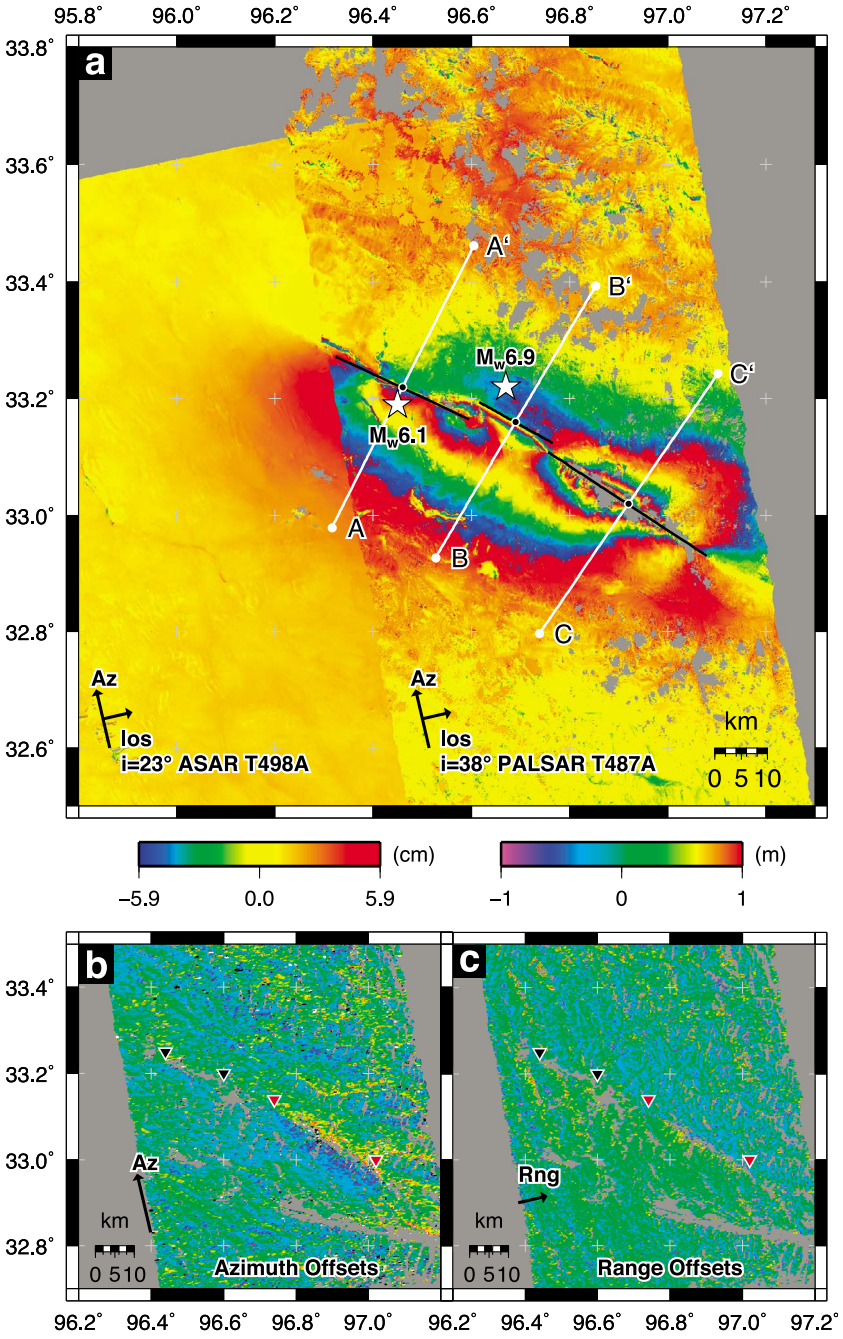

Figure 2. (a) Mosaic of ascending interferograms ASAR T498 and PALSAR T487. Interferograms are wrapped to 11.8 cm fringes (left-hand color scale – blue through yellow to red indicating motion away from the satellite along the line-of-sight). The ASAR image is offset to match the far-field zero of the PALSAR, resulting in a slight mismatch in the fringes in the near-field as the look direction for the two acquisitions is different. White stars indicate the NEIC epicenters for the main shock (M_w 6.9) and aftershock (M_w 6.1). Solid lines indicate the three fault segments used in the modeling. White lines A-C indicate profiles shown in Figure 4. (b) PALSAR T487 azimuth displacements which indicate motion along the flight direction NNW. Over ±0.5 m of azimuth displacement is observed for the southeastern segment (right-hand color scale – positive indicates motion in the NNW direction). The red arrowheads represent the segments that the fault clearly ruptured the surface while black arrowheads denote the other segments without a clear rupture on the surface. Note the line of decorrelation that marks out the fault. (c) PALSAR T487 range displacements (positive indicates that the surface moves away from satellite). North of the fault, motion is toward the satellite, south of the fault motion is away.

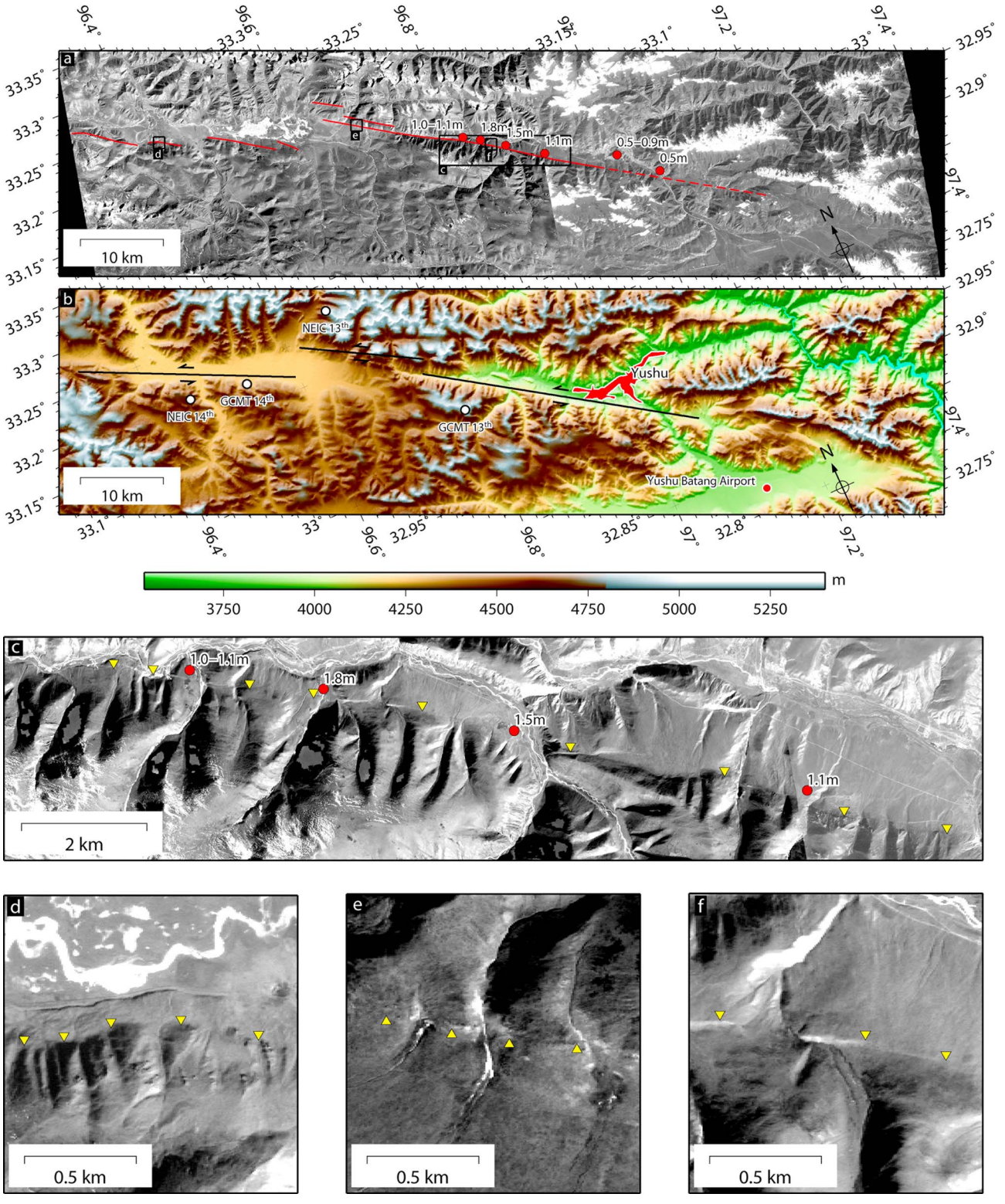
a
b
c
d
e
f
1.0–1.1m
1.8m
1.5m
1.1m
0.5–0.9m
0.5m
NEIC 13th
NEIC 14th
GCMT 14th
GCMT 13th
Yushu
Yushu Batang Airport
10 km
2 km
0.5 km
N
m
3750
4000
4250
4500
4750
5000
5250

Figure 3

in azimuth. All are located at teleseismic distances to avoid complications from the Earth's crust and core. We model *P*, *pP* and *sP* phases on vertical component seismograms restricted to the epicentral distance range 30°–90°, and *S* and *sS* phases on transverse components in the range 30°–80°. The MT5 program [*Zwick et al.*, 1994] was used to invert the P and SH waveforms for strike, dip, rake, centroid depth, seismic moment and source time function of the best double-couple solutions (Table 1 and Figure 5). We follow the procedure described by *Molnar and Lyon-Caen* [1989], using a weighted least squares method [*McCaffrey and Abers*, 1988]. Amplitudes are corrected for geometrical spreading, and for anelastic attenuation using Futterman operators with a t^* of 1.0 s and 4.0 s for *P* and *SH* waves respectively. We use a simple half-space source velocity model, with velocities, densities and Lamé elastic constants that match those used for the InSAR elastic modeling.

[19] The optimal solution yields a 117° striking, 77° southwest-dipping fault with a centroid depth of 6 km, and a predominately left-lateral component of slip (Table 1), consistent with other catalog solutions, but with a significantly shallower centroid depth. A clear directivity effect was observed in the body wave seismograms, particularly in the SH waves, and the fit of observed to synthetic waveforms was significantly improved by allowing for a southeastward (120°) rupture propagation at 2.5 km/s, though this speed itself is not well resolved.

3. Determining the Fault Geometry and Slip Distribution

[20] The data sets used in the modeling comprise one ascending PALSAR and two ASAR interferograms (one ascending, one descending). Taking into account the high spatial correlation of pixels and to expedite the modeling process, interferograms were downsampled to create more manageable data sets with a modified resolution-based decomposition algorithm [*Lohman and Simons*, 2005]. This reduced the number of data points in the inversion from millions to thousands (Table 2). Due to the slightly curved and stepping geometry of the real fault trace, some data points are on the wrong side of our simplified fault plane model. Therefore data points within 2 km of the fault trace were removed in our modeling.

3.1. Uniform Slip Model

[21] In order to simplify the overall, complex surface pattern of the fault on which the Yushu earthquake occurred, three straight line segments are fitted to the surface trace based upon our observations from the SAR data sets and SPOT images (Figures 2 and 3). The straight line segment for the southeastern segment is never more than 500 m from the fault trace in the SPOT images. On the central and northwestern segments, where the fault trace on the SPOT images has multiple strands or en-echelon sections, the departures from a straight line can be up to 1–2 km, although they are generally less than this.

[22] The interferometric phase was then modeled as that due to uniform slip on the three rectangular fault segments using an elastic half-space dislocation model [*Okada*, 1992]. An elastic shear modulus of 3.23×10^{10} Pa and a Poisson ratio of 0.25 were used. With the knowledge of the locations of the surface ruptures, the strike angles of the three segments of the Yushu fault were fixed (Table 3). Other fault parameters (including dip, slip, length, top and bottom depth) were determined by minimizing the squared misfits between the observed and the predicted line-of-sight displacements using a hybrid minimization algorithm [*Feng and Li*, 2010] that combines Particle Swarm Optimization (PSO) [*Eberhart and Kennedy*, 1995] and the downhill simplex algorithm (DSA) [*Nelder and Mead*, 1965]: (1) PSO is employed to perform a global search to find several local minima; (2) based on the PSO-derived local minima, DSA is then used to determine the global minimum.

[23] Table 3 shows the optimal geometry determined in this way. The SE and NW segments are near vertical, but the central segment dips 70° to the southwest. The rakes indicate almost pure left-lateral slip, the greatest of which occurs on the SE segment (1.25 m). Top depths show that slip approached the surface for the SE and NW portions of the fault. The bottom depths of the fault segments are 8–13 km, indicating that slip is constrained to the uppermost crust.

[24] To determine parameter errors for the nonlinear PSO/simplex integrated inversion (Table 3), a Monte Carlo simulation of correlated noise was used [*Funning et al.*, 2005; *Li et al.*, 2008; *Parsons et al.*, 2006; *Wright et al.*, 2003]. A 1-D covariance function was estimated using a far-field area of the interferogram where there is no deformation signal from the earthquake. Using a variance-covariance matrix for the sampled data points, 100 sets of correlated noise were simulated to create 100 perturbed data sets. We apply the inversion procedure to each of these data sets and the distribution of best fitting solutions provides information on parameter errors and their trade-offs (Figures S3–S5). Several strong trade-offs between different model parameters are observed: such as between the slip and the minimum depth for

Figure 3. (a) Composite of 2 SPOT 5 pre-earthquake satellite images (25/12/2007 and 05/11/2009) covering the Yushu-Garze fault. The image is in an oblique Mercator projection with the oblique equator coincident with the mean trace of the fault. Red lines delineate fault segments mapped from the SPOT data, and red circles and associated labels show the location and magnitude of coseismic left-lateral surface ruptures mapped in the field by *Chen et al.* [2010]. The dashed red line shows the inferred fault where no clear surface features nor stream offsets are visible. Black boxes show locations of Figures 3c–3f. Illumination in the image is from the SE, in a direction close to the strike of the fault. (b) Shaded relief using SRTM 3 arc-second topography for the same area as in Figure 3a. Artificial illumination is from the north in this case. The fault extents for the three segments used in the distributed slip model (Figure 6) are delineated as black lines. The epicenters as recorded by the USGS NEIC and centroid locations from the GCMT are marked as white circles. The extent of the urban area of the town of Yushu is marked in red, as is the location of the new airport. (c–f) Enlargements of the parts of the SPOT 5 image of the Yushu-Garze fault indicated by boxes in Figure 3a, shown in the same projection. Yellow triangles point to the trace of the fault mapped from the SPOT data, and red circles and associated labels are the same as in Figure 3a. Figures 3c, 3d, and 3e show areas on the SE, NW and Central sections of the fault trace, respectively, with Figure 3f showing a small part of Figure 3c.

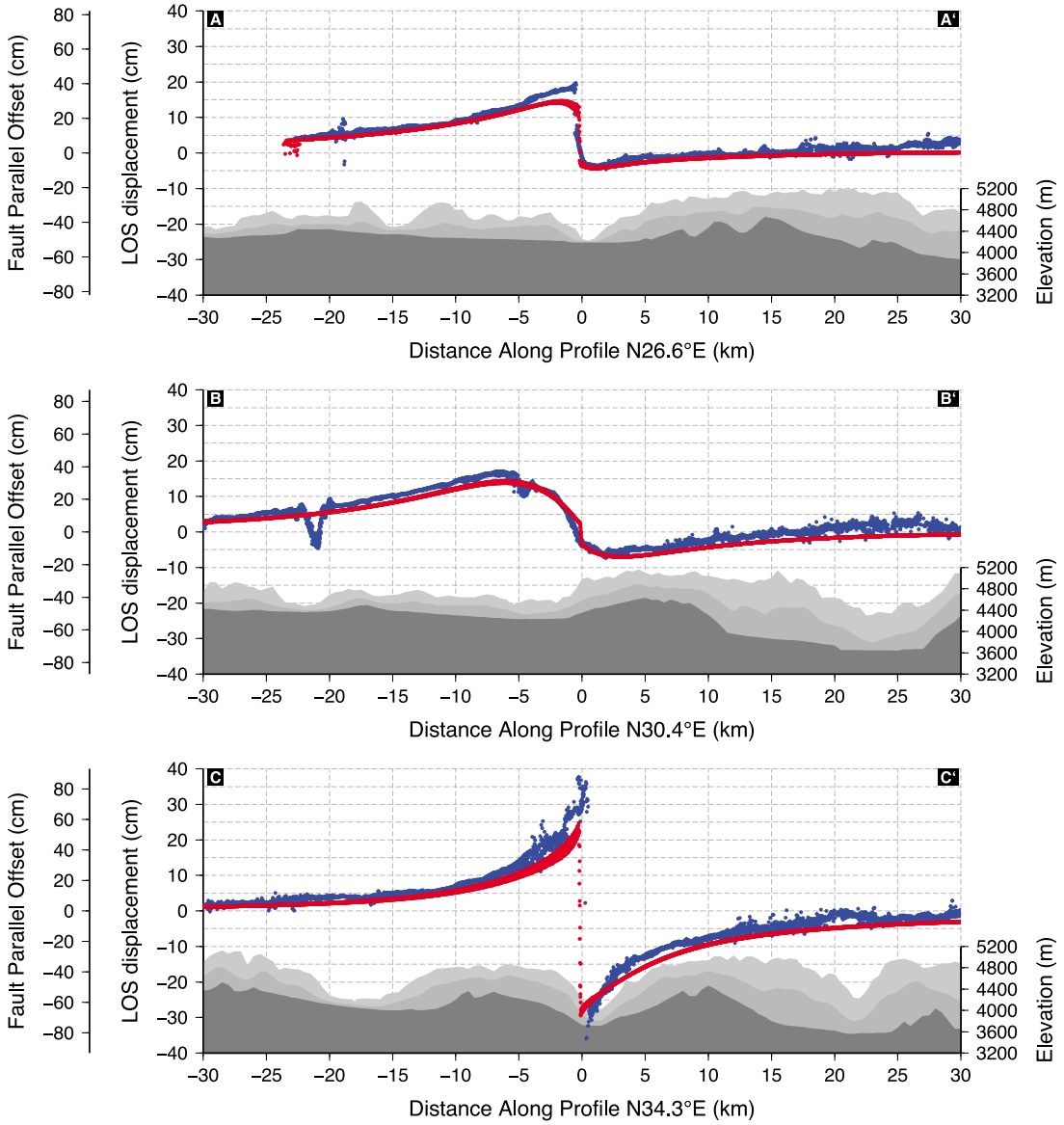

Figure 4. Profiles of line-of-sight (LOS) displacements (blue dots), model LOS displacements (red dots) and topography (gray) taken perpendicular to the individual strikes of the three segments, midway along their lengths. The inferred fault parallel offset is shown as an offset axis on the left, assuming that the line-of-sight displacement is purely fault-parallel horizontal motion. An inferred left-lateral offset of up to 1.6 m is seen in profile C-C′ (southeastern segment). The locations of profiles A-A′, B-B′ and C-C′ are shown in Figures 2 and 6. Note the profiles are created with swaths that are ±0.5 km for the interferogram data (blue) and slip distributed model (red). The topography is taken in ±5 km swaths giving minimum (dark gray), mean (gray) and maximum (light gray) profiles.

the NW segment, as the model struggles to fit the near-surface displacements with uniform slip at depth. Also there is a tradeoff between the slip and the rake for the SE segment, and tradeoffs between the moment and the maximum depth occur for all three segments.

[25] Figure 6 shows the interferograms for the ascending tracks predicted by the optimal uniform-slip model, and the residuals with respect to the InSAR observations. (Figure S2 shows the descending interferogram and model.) It is clear that the uniform model is consistent with the InSAR displacements and produces a first order fit to the observed deformation pattern with a small root mean square (RMS) misfit: 0.5 cm to ASAR T498A, 1.2 cm to ASAR T004D, and 1.8 cm to ALOS T487A interferograms. However, a significant number of residual fringes are observed close to the fault. There are two probable causes for these residuals in the near field: (1) the simplified fault plane model fails to reproduce high fringe gradients close to the fault, and (2) the removal of data points within 2 km of the fault trace reduces the coverage of such high-gradient areas. A simple elastic dislocation generally lacks the capability to model near-fault processes, which has also been evidenced by several previous InSAR studies [e.g., *Funning et al.*, 2007; *Lohman and Simons*, 2005].

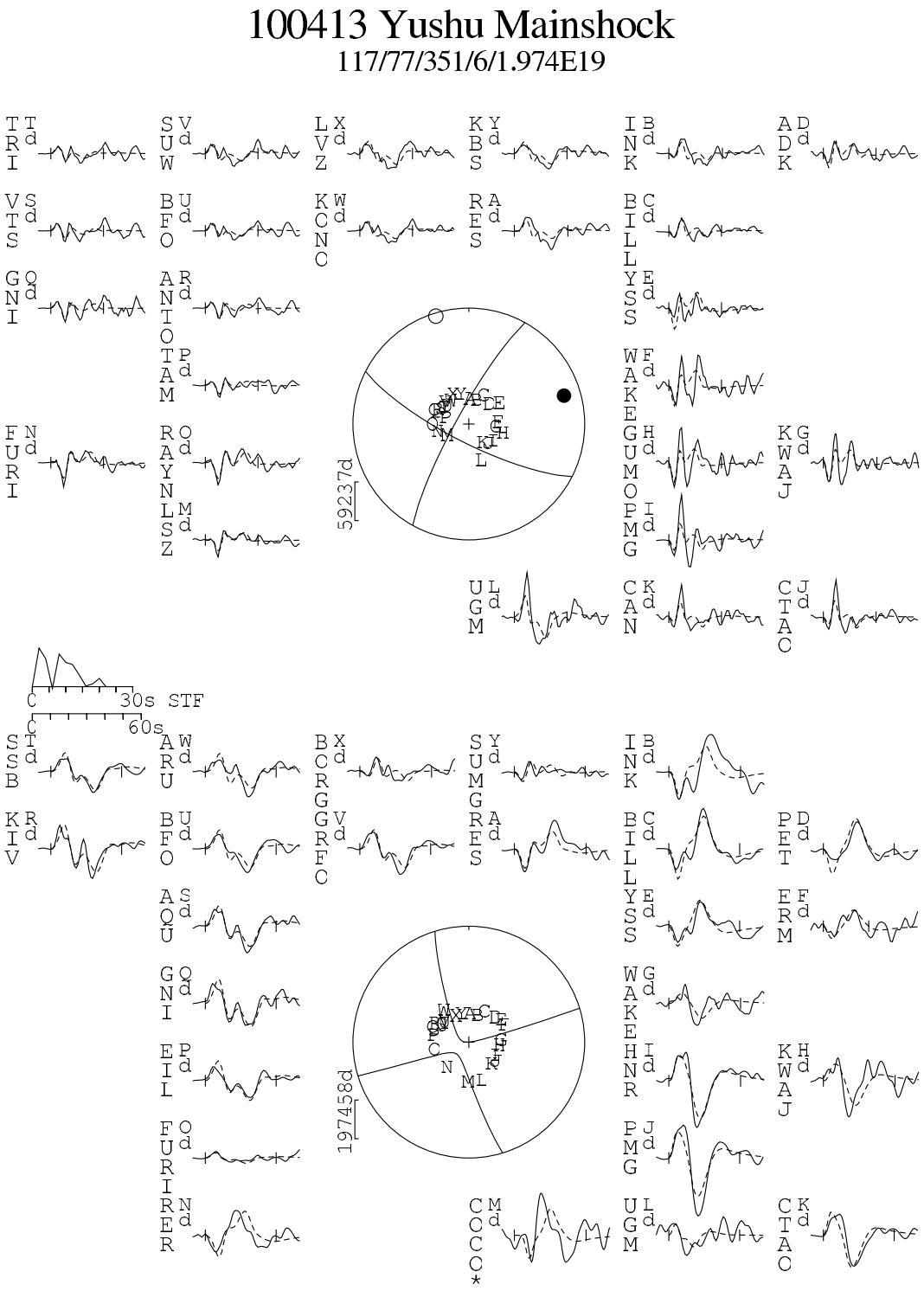

Figure 5. Focal mechanisms show (top) P and (bottom) SH nodal planes in a lower hemisphere projection. Closed and open circles represent the P- and T- axes respectively. Waveforms for each station are plotted around the focal mechanisms in their approximate azimuthal locations. Observed waveforms are solid and synthetic waveforms are dashed, while the vertical ticks mark the inversion window. The station code is to the left of each waveform, in vertical capital letters. The vertical bar and number beside each focal sphere is the amplitude scale for the plotted seismograms (in μm). STF is the source time function, and the scale bar below it is the horizontal scale for the seismograms. The numbers in the header are strike, dip, rake, centroid depth (km), and moment (N m) for the best fit solution.

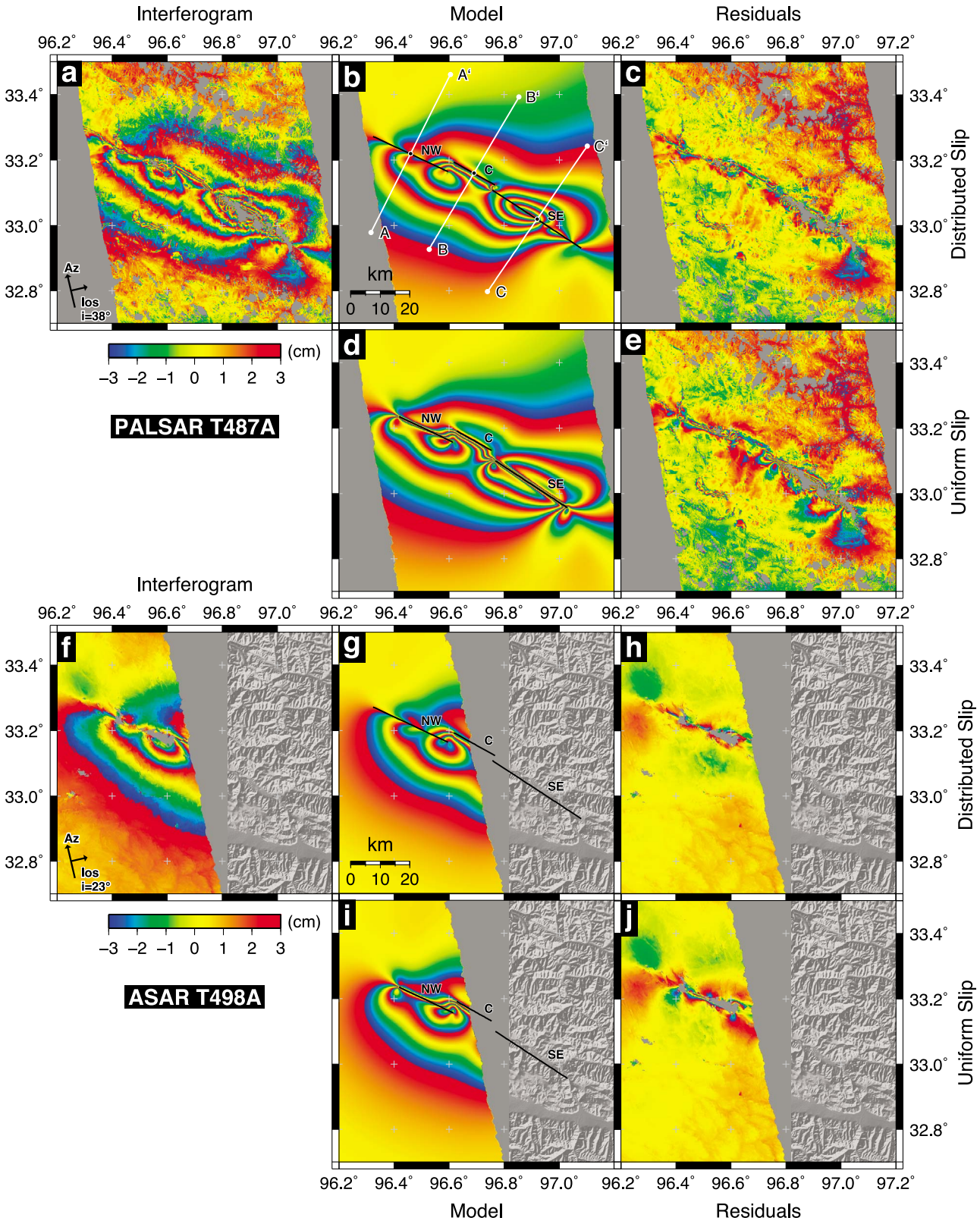
Interferogram
Model
Residuals
Distributed Slip
Uniform Slip
PALSAR T487A
ASAR T498A
(cm)
km
NW
C
SE
A
A'
B
B'
C
C'
Az
los
i=38°
i=23°

Figure 6

Table 3. Source Fault Parameters and Their 1σ Confidence Limits for the Uniform Slip Model Comprising Three Sub-Faults[a]

Fault segment	Strike (deg)	Dip (deg)	Rake (deg)	Latitude (deg)	Longitude (deg)	Length (km)	Slip (m)	Top (km)	Bottom (km)	Moment (10^{18} Nm)	M_w
1 (NW)	116.6*	87.9 ± 3.3	2.7 ± 1.7	33.1962*	96.5163*	20.2 ± 0.7	0.70 ± 0.07	0.6 ± 0.1	8.3 ± 1.2	3.51 ± 0.43	6.30
2 (C)	120.4*	69.5 ± 6.2	−2.6 ± 2.2	33.1615*	96.6908*	13.6*	0.85 ± 0.11	1.6 ± 0.3	12.9 ± 1.6	4.49 ± 0.56	6.37
3 (SE)	124.3*	89.4 ± 2.9	0.2 ± 2.0	33.0281*	96.8988*	29.2 ± 1.1	1.25 ± 0.08	0.5 ± 0.03	10.0 ± 1.3	11.17 ± 1.10	6.63
Total						63 ± 1.3				19.17 ± 1.31	6.79

[a]The latitude and longitude are for the vertical projection of the fault center to the surface. The parameters denoted by an asterisk are fixed to those derived from other observations. Formal 1σ errors of model fault parameters are determined using a Monte Carlo method [*Wright et al.*, 2003]. See Figure S4 for full uncertainties and trade-offs.

3.2. Distributed Slip Model

[26] Once the orientations of the fault planes have been determined, the model can be further refined by solving for the distribution of slip on the fault. Using the fault geometry determined in the uniform slip modeling, we extended the Yushu fault plane along strike and downdip by increasing its total length to 80 km and downdip width to 20 km, and then divided the fault into 1600 sub-faults each measuring 1 km by 1 km. The best fitting values of strike-slip and dip-slip motion for each sub-fault were solved for in a least squares sense, while Laplacian smoothing and a nonnegative least squares algorithm were employed to prevent unphysical oscillatory slip [*Feng and Li*, 2010; *Funning et al.*, 2005; *Wright et al.*, 2003]. The perturbed data sets used for the Monte Carlo analysis were also employed to produce 100 slip distribution maps and standard deviations (Figure 7). For the vast majority of fault patches, the errors are a small fraction of the magnitude of the slip. However, for the deeper fault patches on the central segment and the most northwesterly parts of the northwestern segment, the errors approach 25 cm. This indicates that the apparent slip in these regions is most likely to be due to noise in the interferograms and the large component of dip-slip behavior in these areas is probably an artifact. The values of slip and errors for each fault patch in Figure 7 are tabulated in the auxiliary material (Data Sets S1–S6).

[27] The calculated slip distribution images three areas of high slip (asperities) greater than 0.5 m (Figure 7), and significant slip is observed to occur along strike for almost 80 km. The greatest magnitude of 1.5 m left-lateral slip occurs on the SE segment at a depth of 4 km, with motion constrained largely to the upper 10 km of the crust. The 30 km length of significant (>0.5 m) near-surface slip in the model on this segment matches well the field observation of surface ruptures running for 31 km.

[28] The second largest slip patch occurs on the central, southwesterly dipping segment, where up to 1.25 m of largely strike-slip motion is observed to peak at 8 km, but with significant slip down to 18 km, deeper than for the other segments. The model does, however, predict very little near-surface slip, as supported by the lack of such observations in the SAR range and azimuth displacements and field investigations. It is difficult to determine if the dip-slip component at 10–18 km depth for the southeastern half of the central segment is significant (Figure 7b). This region lies in the area estimated to have the largest uncertainty (1 sigma errors of up to 30 cm; Figure 7e) and which is largely in the dip-slip direction. This error could arise from far-field noise (as seen in the topographically correlated residuals tracing out the valleys to the north of the fault in Figure 6c), trade-offs with orbital parameters or due to the step in the fault model to the southeastern segment.

[29] The NW segment has over 0.75 m slip at 6 km depth, with motion constrained to the upper 10 km of the model. Interestingly, significant near-surface slip is predicted in the upper 1 km of the model, suggesting that up to 50 cm of left-lateral offset might be observable in the field over a distance of a few kilometers.

[30] It is clear in Figure 6b that the maximum moment release is at a depth of 5 km, with much of the release occurring above depths of 10–15 km. The seismic moments increase from NW to SE: 4.6×10^{18} N m in the NW section, 6.9×10^{18} N m in the central section, and 10.1×10^{18} Nm in the SE section.

[31] The variable-slip model shows an improved fit in the near field, with an RMS misfit of 1.6 cm to the ALOS T487A interferograms (Figure 6c) compared with 1.8 cm for the uniform slip model (Figure 6e). The fringe pattern of the distributed slip model does appear to be closer to that of the observed signals; particularly in the region along the projection of the fault segments at the surface. Similar improvements are seen for the northwestern segment covered by the ASAR T498 interferogram. Moreover, the distributed slip model seismic moment of 2.2×10^{19} Nm agrees better with the GCMT moment (2.5×10^{19} Nm) than the uniform

Figure 6. (a) PALSAR T487A interferogram with line-of-sight deformation wrapped to 6 cm fringes, with each cycle from blue through yellow to red indicating motion away from the satellite in the direction indicated by the arrow in the lower right-hand corner. (b) Interferogram model and (c) residuals based upon the three fault segment (black lines) slip distribution shown in Figure 7. White lines A-A′, B-B′ and C-C′ refer to profiles taken perpendicular to each fault segment through its midpoint and shown in Figure 4. (d) Interferogram model and (e) residuals based upon the uniform slip model for the three segments (black lines) with fault parameters given in Table 3. The move from a uniform to distributed slip model shows an improvement in the near fault fit to the interferogram, as indicated in the residual plots which show fewer fringes close to the faults for the distributed slip case (Figure 6c). (f) ENVISAT ASAR T498A interferogram. (g) Interferogram model and (h) residuals based upon the three fault segment (black lines) slip distribution shown in Figure 7. (i) Interferogram model and (j) residuals based upon the uniform slip model for three segments (black lines) with fault parameters given in Table 3.

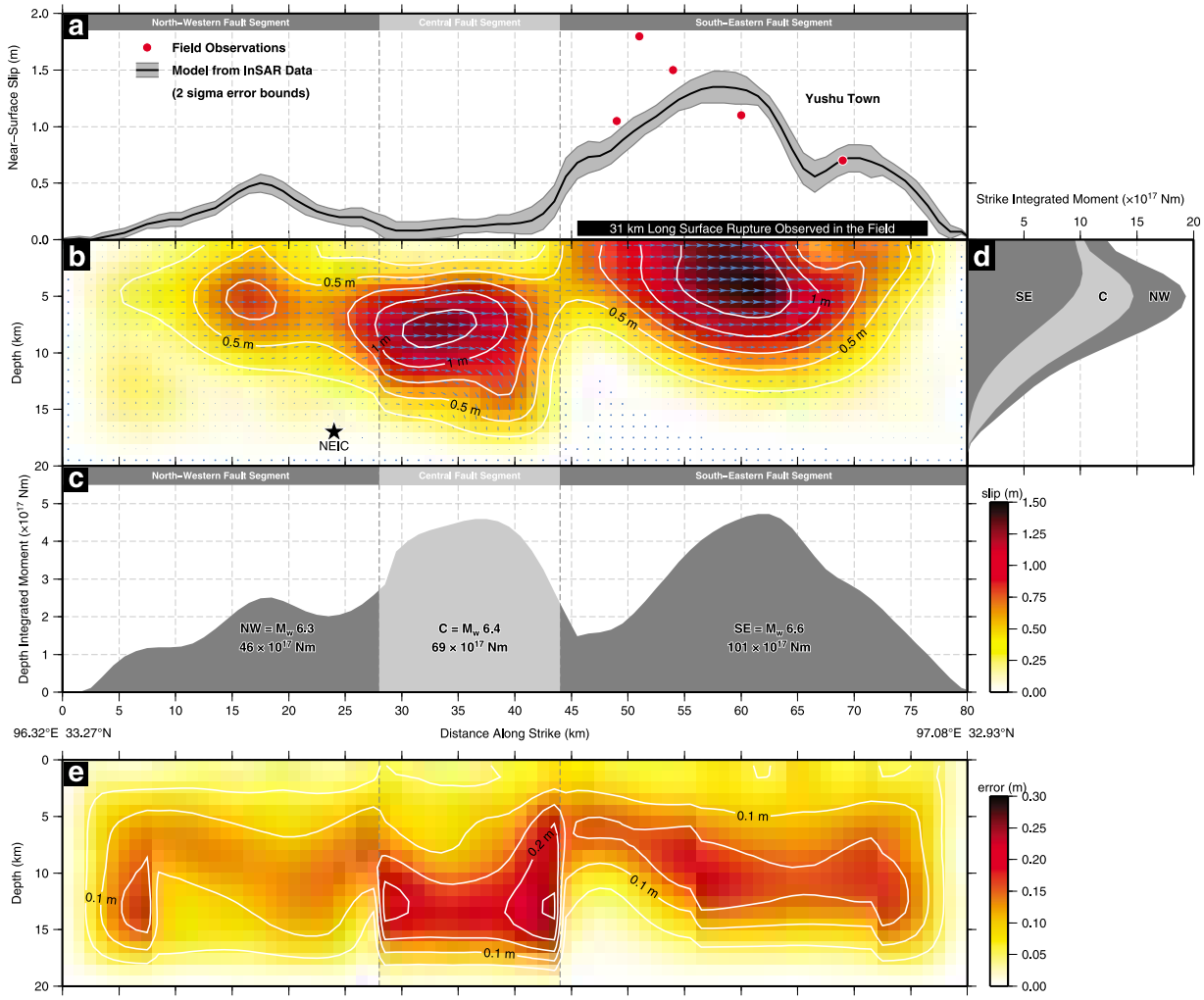

Figure 7. (a) Predicted surface slip and 2 sigma error bounds based upon the top 1 km of the distributed slip model and Monte Carlo errors. The five field observations of left-lateral slip from *Chen et al.* [2010] are indicated by red circles and the 31 km long surface rupture is indicated by the black bar. The location of the town of Yushu (Gyegu) just on the northern side of the southeastern segment is also shown. (b) Slip distribution model for 3 sub-faults projected onto a vertical plane 80 km long and 20 km wide. The color scale indicates the magnitude of slip. Slip is also contoured at 0.5 m intervals. Blue slip vectors indicate the motion of the hanging wall with respect to the footwall. The black star is the projection of the NEIC epicenter onto the fault plane. (c) Depth integrated moment along strike of the fault. The total moment and moment magnitude is given for the 3 subfaults: North-Western (NW), Central (C) and South-Eastern (SE). The fault end coordinates are given at the bottom. (d) Along-strike integrated moment for the 3 sub faults. Eighty per cent of the moment is released in the upper 10 km of the crust. (e) Error in the distributed slip calculated from the standard deviation of the slip distributions obtained by inverting 100 perturbed interferograms. The color scale is one fifth of the interval used for the slip panel. For most fault patches the fractional error is small. However, the error on the deeper parts of the central segment indicates that the slip in this region is poorly resolved and that the dip-slip component is likely to be an artifact of noise in the interferograms.

model moment (1.9×10^{19} Nm), although it is 10% higher than the body wave solution (2.0×10^{19} Nm).

4. Discussion

4.1. Estimates of the Fault Length

[32] Field observations made after the earthquake discovered surface ruptures over a length of 31 km. *Wells and Coppersmith* [1994] give an empirical relationship between surface rupture length (L_{sr}, in km) and moment magnitude (M_w) derived from observations of 43 strike-slip faults ($5.6 < M_w < 8.1$),

$$\log_{10} L_{sr} = -3.55 + 0.74 \times M_w$$

With $M_w = 6.8$, this gives a surface rupture length of 30 km. In addition, a back-of-the-envelope estimate of fault length can be made from the seismic moment

$$M_0 = \mu A \bar{s} = \mu W L \bar{s}$$

where μ is the elastic modulus of rigidity, A the area of the fault rupture, W the downdip width of the fault, L the length of the rupture, and $\bar{s}$ is the mean slip on the fault. Taking the GCMT value for M_0 of 2.5×10^{19} N m, a value for μ of 3.2×10^{10} Pa, assuming the rupture broke the whole of a seismogenic layer 15 km thick and that $\bar{s}$ was equal to the observed values at the surface (~1.5 m), an estimate for the length of the fault of 35 km is obtained.

[33] The consistency of these estimates initially suggested that the fault length was 30–35 km. However, the radar interferograms (Figures 2 and 6) immediately showed that the rupture at depth must have occurred over an extent closer to 80 km. The difference between these observations suggests that the distribution of slip and hence moment release should be looked at in more detail.

4.2. Distribution of Slip and Moment Release

[34] The slip distribution on the 3 sub-faults is able to reproduce the main features of the observations with a RMS residual of ≤1.6 cm. Three asperities with slip greater than 0.5 m can be identified within the slip pattern, and the largest one with a peak of ~1.5 m of slip at a depth of 3–5 km is located beneath the places where the surface ruptures were observed (Figure 7b).

[35] The seismic moment release due to each 1 × 1 km fault patch was summed in vertical columns to give the variation of moment release with distance along the fault (Figure 7c), and summed in horizontal rows to give the variation in moment release with depth (Figure 7d). About 80% of the moment is released for depths shallower than 10 km. This depth interval is similar to that observed for strike-slip faults elsewhere in Tibet, e.g., the 1997 Manyi earthquake [*Funning et al.*, 2007].

[36] Taking a downdip fault width of 10 km, the estimate of fault length becomes 52 km with the GCMT moment or 42 km with the moment of 2.2×10^{19} N m from the body wave modeling. These estimates are close to the combined length of 50 km of the central and southeastern segments of the fault.

4.3. Source Time Function and Moment Release

[37] The source time function from the body wave modeling consists of two peaks (Figure 5), the first 6 s long and the second 14 s. The central and southeastern patches of moment release (Figure 7b) are likely to correspond to the two peaks in the source time function determined by the body wave modeling, in which a southeastward rupture propagation effect was observed. The lengths of the moment-release patches along strike (~15 km and ~35 km) are consistent with the widths of the two peaks in the source time function at this rupture speed.

[38] The extensive damage to the town of Yushu is likely to be due to its location at the end of the fault in the direction of rupture propagation. The directivity effect leads to a dramatic enhancement of the SH pulse, which is perpendicular to the fault and rupture propagation, producing horizontal ground motions that are particularly destructive [*Bouchon et al.*, 2006]. This relative location of town and rupture direction is very similar to that in the 2003 Bam (Iran) earthquake [*Bouchon et al.*, 2006; *Jackson et al.*, 2006]. In this case, however, there are no strong motion instruments to confirm the above hypothesis or to precisely locate the position of rupture initiation.

4.4. Relative Aftershock Location

[39] The observations in the previous two sections suggest that the moment release in the main event can be accounted for by that of the central and southeastern segments, and that perhaps the moment release in the northwestern segment results from the aftershock that happened 95 min after the main shock (Table 1). To determine whether the aftershock could have reasonably occurred on the fault segment to the northwest of the main epicenter, we examined the difference in travel times of the P wave for the two events, measured relative to the mean travel time difference, at the seismic stations shown in Figure 8b.

[40] It was observed that, at stations lying in the northwest quadrant relative to the epicenter, the P waves arrived 0–1.3 s earlier for the aftershock than for the main shock (Figure 8a). The converse was true for stations in the southwest quadrant where the aftershock P wave travel times were 0–1.4 s longer. This observation, and the fact that the moment magnitude corresponding to the moment release on the northwest segment equals that of the aftershock, suggest it is likely that the slip on the northwest segment is due to the aftershock.

[41] In Figure 8c, the relative time differences between the main shock and aftershock arrivals are plotted as a function of the sine of the take-off angle (i) for stations with azimuth directions lying within ±20° of the strike of the fault. There is an approximately linear relationship, which is what would be expected if it can be assumed that the epicenters occurred at the same depth. The slope of the line is proportional to the separation of the epicenters. Alternatively, the separation between the epicenters can be estimated on a point-by-point basis (Figure 8d). A crustal velocity of 6.6 km/s was used to convert times to distances. There is quite a spread in the estimated separation due to the difficulty in picking the two

Figure 8. (a) Difference in seconds between the P wave travel times for the aftershock on the 14th and those for the main shock 2 h prior as a function of the azimuth for 35 WWSSN stations in the epicentral distance range of 10–90°. The travel time difference plotted for each station is relative to the mean travel time difference for all stations. Those stations for which the aftershock P-arrival was relatively early are colored red; those for which a relatively late arrival occurs are in blue. The solid red line denotes the strike of the Yushu fault, and the dashed lines define a ±20° azimuth range about the strike direction. (b) Distribution of reporting WWSSN seismological stations (red triangles) for which P arrivals could be picked in the epicentral distance range of 10–90° about the location of the Yushu earthquake (yellow star). (c) The time delay between the aftershock and main shock versus the *sine* of the take off angle (i) for the 15 stations with an azimuth direction within ±20° of the fault strike as denoted in Figure 8a. The plot shows an approximately linear relationship. Assuming the earthquakes originated at the same depth and using a P wave velocity for the crust of 6.6 km/s, the time differences can be converted to an extra path length traveled by the rays (right-hand axis). (d) Histogram of separation between epicenters estimated from the relative travel time difference for each of the 15 stations. The mean separation is 11 km.

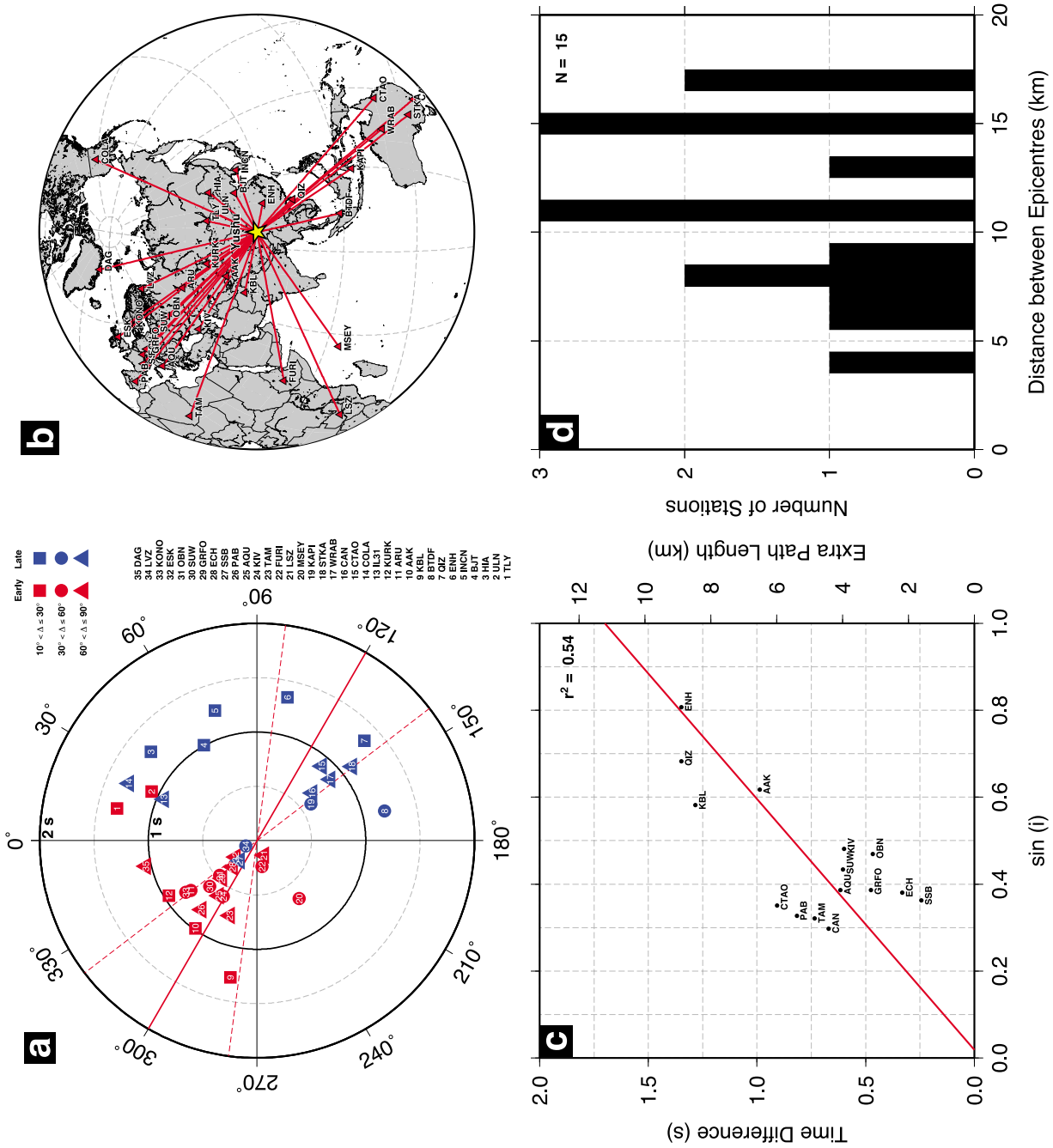
a
b
c
d
Early
Late
10° < Δ ≤ 30°
30° < Δ ≤ 60°
60° < Δ ≤ 90°
1 s
2 s
35 DAG
34 LVZ
33 KONO
32 ESK
31 OBN
30 SUW
29 GRFO
28 ECH
27 SSB
26 PAB
25 AQU
24 KIV
23 TAM
22 FURI
21 LSZ
20 MSEY
19 KAPI
18 STKA
17 WRAB
16 CAN
15 CTAO
14 COLA
13 IL31
12 KURK
11 ARU
10 AAK
9 KBL
8 BTDF
7 QIZ
6 ENH
5 HON
4 BJT
3 HIA
2 ULN
1 TLY
Time Difference (s)
sin (i)
r² = 0.54
Extra Path Length (km)
Number of Stations
N = 15
Distance between Epicentres (km)

Figure 8

P-arrivals to an accuracy of less than 1 s, but the mean estimate for the 15 stations is 11 km, in agreement with the estimate from the slope in Figure 8c.

4.5. Faulting Characteristics

[42] These observations support the interpretation that the northwestern segment (Figure 7b) most likely ruptured in the aftershock 95 min after the main event. Neglecting the contribution of 4×10^{18} N m to the moment from the northwestern segment, the distributed slip model gives a geodetic moment of 1.7×10^{19} N m, in reasonable agreement with the body wave seismic moment of 2.0×10^{19} N m.

[43] Assuming a fault length of 50 km, i.e., the length of the central and southeastern segments of the fault, and a downdip width of 10 km, the mean slip $\bar{s}$ is 1.1 m, with a slip-to-length ratio ($\bar{s}/L$) of 2.1×10^{-5}. The latter is in the middle of the range of values observed for strike-slip earthquakes, e.g., it is twice that for the 1997 Manyi and 2001 Kokoxili earthquakes [*Funning et al.*, 2007; *Lasserre et al.*, 2005], also in Tibet, and half that of the Bam earthquake [*Funning et al.*, 2005].

[44] *Wells and Coppersmith* [1994] found that the length of the rupture at the surface is generally 75% of the subsurface length. For Yushu this value is 60%, and it may be preferable to regard the earthquake as two sub-events on fault segments with different characteristics. On the southeastern segment, where the surface ruptures occurred, the fault trace follows a valley with a relief of over 1 km. In contrast, on the central segment where faulting did not reach the surface, there is no valley and the fault follows a mountain front.

4.6. Seismic Hazard for Yushu

[45] The topographic expression of the Yushu fault continues southeast beyond the town of Yushu, running north of the new airport (Figure 3). This portion of the fault remains unruptured (Figure 7) and given the last event on this segment is likely to have been over 100 years ago [*Wen et al.*, 2003], there remains a continuing seismic hazard for the town. Assuming a rate of strain accumulation of 7 mm/yr for this portion of fault [*Zhou et al.*, 1996] implies a deficit of slip equal to 0.7 m over this period. This deficit is equivalent to a magnitude 6.5 earthquake, if it were to be released seismically on a similar sized fault as the SE segment, i.e., in a rupture 10 km wide and 35 km long.

5. Conclusions

[46] We have combined SAR and optical imagery, interferometric phase and coherence measurements, and body wave seismology to constrain the fault geometry and slip distribution for the 2010 M_w 6.8 Yushu (China) earthquake. We find that:

[47] (1) Nearly pure left-lateral slip has occurred on three segments of the Yushu fault over a distance of nearly 80 km, with maximum slip of 1.5 m on the 30 km long southeastern segment.

[48] (2) The northwestern and southeastern segments of the fault are near vertical, but the central segment appears to dip 70° to the southwest. The fault rupture broke the surface along the southeast segment and came close to the surface on the northwest segment, on both of which the fault follows a valley with relief of over 1 km. There is no surface break on the central segment, where the fault trace follows a mountain front.

[49] (3) The slip on the northwestern segment is probably due to the M_w 6.1 aftershock that occurred just under 2 h after the main shock.

[50] (4) Almost eighty per cent of the moment release occurred for depths less than 10 km. The mean slip over the combined 50 km length of the central and southeastern segments is 1.1 m.

[51] (5) The considerable building damage can be accounted for by the fact that the rupture in the main shock propagated at a speed of 2.5 km/s toward the town of Yushu located at the end of the southeastern segment of the fault. Strain accumulation since the last earthquake on the continuation of the fault beyond Yushu has the potential to produce an M_w 6.5 event.

[52] **Acknowledgments.** This work was supported by the Natural Environmental Research Council (NERC) through the GAS project (NE/H001085/1) and the National Centre of Earth Observation (NCEO), of which the Centre for the Observation and Modeling of Earthquakes, Volcanoes and Tectonics (COMET+, http://comet.nerc.ac.uk) is a part. Part of this work was supported by a China NSFC project (41074005) and a China 863 project (2009AA12Z317). All ENVISAT SAR data are copyrighted by the European Space Agency and were provided under project AOE-621 and through the ESA-MOST Dragon 2 Cooperation Program (ID: 5343). All ALOS data are copyrighted by JAXA. We are grateful to JPL/Caltech for use of the ROI_PAC software. We would like to thank Ivana Barisin for orthorectifying the SPOT satellite imagery, courtesy of SPOT Image, and David Robinson for his help with the seismic analysis. Most figures were made using the public domain Generic Mapping Tools [*Wessel and Smith*, 1998].

References

Bouchon, M., D. Hatzfeld, J. A. Jackson, and E. Haghshenas (2006), Some insight on why Bam (Iran) was destroyed by an earthquake of relatively moderate size, *Geophys. Res. Lett.*, *33*, L09309, doi:10.1029/2006GL025906.

Chen, C. W., and H. A. Zebker (2000), Network approaches to two-dimensional phase unwrapping: Intractability and two new algorithms, *J. Opt. Soc. Am. A Opt. Image Sci. Vis.*, *17*, 401–414, doi:10.1364/JOSAA.17.000401.

Chen, L., H. Wang, Y. Ran, X. Sun, G. Su, J. Wang, X. Tan, Z. Li, and X. Zhang (2010), The Ms7.1 Yushu earthquake surface ruptures and historical earthquakes, *Chin. Sci. Bull.*, *55*(13), 1200–1205.

Eberhart, R. C., and J. Kennedy (1995), A new optimizer using particle swarm theory, Proceedings of the Sixth International Symposium on Micro Machine and Human Science, pp. 39–43, Inst. of Electr. and Electron. Eng., Piscataway, N. J., doi:10.1109/MHS.1995.494215.

Feng, W., and Z. Li (2010), A novel hybrid PSO/simplex algorithm for determining earthquake source parameters using InSAR observations, *Prog. Geophys.*, *25*(4), 1189–1196.

Funning, G. J., B. Parsons, T. J. Wright, J. A. Jackson, and E. J. Fielding (2005), Surface displacements and source parameters of the 2003 Bam (Iran) earthquake from Envisat advanced synthetic aperture radar imagery, *J. Geophys. Res.*, *110*, B09406, doi:10.1029/2004JB003338.

Funning, G., B. Parsons, and T. J. Wright (2007), The 1997 Manyi (Tibet) earthquake: Linear elastic modelling of coseismic displacements, *Geophys. J. Int.*, *169*, 988–1008, doi:10.1111/j.1365-246X.2006.03318.x.

Gan, W., P. Zhang, Z.-K. Shen, Z. Niu, M. Wang, Y. Wan, D. Zhou, and J. Cheng (2007), Present-day crustal motion within the Tibetan Plateau inferred from GPS measurements, *J. Geophys. Res.*, *112*, B08416, doi:10.1029/2005JB004120.

Jackson, J., et al. (2006), Seismotectonic, ruptureprocess, and earthquake-hazard aspects of the 26 December 2003 Bam, Iran, earthquake, *Geophys. J. Int.*, *166*, 1270–1292, doi:10.1111/j.1365-246X.2006.03056.x.

Jarvis, A., H. I. Reuter, A. Nelson, and E. Guevara (2008), Hole-filled SRTM for the globe, version 4, http://srtm.csi.cgiar.org, CGIAR Consortium for Spatial Inf.

Lasserre, C., G. Peltzer, F. Crampé, Y. Klinger, J. Van der Woerd, and P. Tapponnier (2005), Coseismic deformation of the 2001 M_w = 7.8 Kokoxili earthquake in Tibet, measured by synthetic aperture radar interferometry, *J. Geophys. Res.*, *110*, B12408, doi:10.1029/2004JB003500.

Li, Z., W. Feng, Z. Xu, P. Cross, and J. Zhang (2008), The 1998 M_W 5.7 Zhangbei-Shangyi (China) earthquake revisited: A buried thrust fault revealed with interferometric synthetic aperture radar, *Geochem. Geophys. Geosyst.*, *9*, Q04026, doi:10.1029/2007GC001910.

Lohman, R. B., and M. Simons (2005), Some thoughts on the use of InSAR data to constrain models of surface deformation: Noise structure and data downsampling, *Geochem. Geophys. Geosyst.*, *6*, Q01007, doi:10.1029/2004GC000841.

McCaffrey, R., and G. Abers (1988), SYN3: A program for inversion of teleseismic body waveforms on microcomputers, *Tech. Rep. AFGL-TR-0099*, Hanscomb Air Force Base, Massachusetts.

Michel, R., J. P. Avouac, and J. Taboury (1999), Measuring ground displacements from SAR amplitude images: Application to the Landers earthquake, *Geophys. Res. Lett.*, *26*(7), 875–878, doi:10.1029/1999GL900138.

Molnar, P., and H. Lyon-Caen (1989), Fault plane solutions of earthquakes and active tectonics of the Tibetan Plateau and its margins, *Geophys. J. Int.*, *99*, 123–154, doi:10.1111/j.1365-246X.1989.tb02020.x.

Nelder, J. A., and R. Mead (1965), A simplex method for function minimization, *Comput. J.*, *7*(4), 308–313.

Okada, Y. (1992), Internal deformation due to shear and tensile faults in a half-space, *Bull. Seismol. Soc. Am.*, *82*(2), 1018–1040.

Parsons, B., T. Wright, P. Rowe, J. Andrews, J. Jackson, R. Walker, M. Khatib, M. Talebian, E. Bergman, and E. R. Engdahl (2006), The 1994 Sefidabeh (eastern Iran) earthquakes revisited: New evidence from satellite radar interferometry and carbonate dating about the growth of an active fold above a blind thrust fault, *Geophys. J. Int.*, *164*(1), 202–217, doi:10.1111/j.1365-246X.2005.02655.x.

Pathier, E., E. J. Fielding, T. J. Wright, R. Walker, B. E. Parsons, and S. Hensley (2006), Displacement field and slip distribution of the 2005 Kashmir earthquake from SAR imagery, *Geophys. Res. Lett.*, *33*, L20310, doi:10.1029/2006GL027193.

Rosen, P. A., S. Hensley, G. Peltzer, and M. Simons (2004), Updated repeat orbit interferometry package released, *Eos Trans. AGU*, *85*(5), 47, doi:10.1029/2004EO050004.

Taylor, M., and A. Yin (2009), Active structures of the Himalayan-Tibetan orogen and their relationships to earthquake distribution, contemporary strain field, and Cenozoic volcanism, *Geosphere*, *5*(3), 199–214, doi:10.1130/GES00217.1.

Wang, H., T. J. Wright, and J. Biggs (2009), Interseismic slip rate of the northwestern Xianshuihe fault from InSAR data, *Geophys. Res. Lett.*, *36*, L03302, doi:10.1029/2008GL036560.

Wells, D. L., and K. J. Coppersmith (1994), New empirical relationships among magnitude, rupture length, rupture width, rupture area, and surface displacement, *Bull. Seismol. Soc. Am.*, *84*(4), 974–1002.

Wen, X., X. Xu, R. Zheng, Y. Xie, and C. Wan (2003), Average slip-rate and recent large earthquake ruptures along the Garzê-Yushu fault, *Sci. China, Ser. D: Earth Sci.*, *46*, suppl. 2, 276–288.

Wessel, P., and W. H. F. Smith (1998), New, improved version of generic mapping tools released, *Eos Trans. AGU*, *79*(47), 579, doi:10.1029/98EO00426.

Wright, T. J., Z. Lu, and C. Wicks (2003), Source model for the M_w 6.7, 23 October 2002, Nenana Mountain Earthquake (Alaska) from InSAR, *Geophys. Res. Lett.*, *30*(18), 1974, doi:10.1029/2003GL018014.

Zhang, Y., L. Xu, and Y. Chen (2010), Fast inversion of rupture process for 14 April 2010 Yushu, Qinghai, earthquake[in Chinese], *Acta Seismol. Sin.*, *32*(3), 361–365.

Zhou, R., S. Ma, and C. Cai (1996), Late quaternary active features of the Ganzi-Yushu fault zone [in Chinese], *Earthquake Res. China*, *12*(3), 250–260.

Zhou, R., X. Wen, C. Chai, and S. Ma (1997), Recent earthquakes and assessment of seismic tendency on the Ganzi-Yushu fault zone, *Seismol. Geol.*, *19*(2), 115–124.

Zwick, P., R. McCaffrey, and C. Abers (1995), Mt5 program, in *Bibliographic References and BSSA Database*, *IASPEI Software Library*, vol. 4, Seismol. Soc. of Am., El Cerrito, Calif.

J. R. Elliott, B. E. Parsons, and R. J. Walters, COMET+, Department of Earth Sciences, University of Oxford, Parks Road, Oxford OX1 3PR, UK.

W. Feng, Institute of Geophysics, China Earthquake Administration, Beijing 100081, China.

J. A. Jackson, COMET+, Department of Earth Sciences, University of Cambridge, Bullard Laboratories, Madingley Road, Cambridge CB3 0EZ, UK.

Z. Li, COMET+, School of Geographical and Earth Sciences, University of Glasgow, East Quandrangle, University Avenue, Glasgow G12 8QQ, UK. (zhenhong.li@glasgow.ac.uk)